A Control Framework for Accurate Mechanical Impedance Rendering with Series-Elastic Joints in Prosthetic Applications

Isaac Harris[1], Elliott Rouse[1], Robert D. Gregg[2], and Gray Cortright Thomas[2*]

Abstract— In addition to lifting up the body during stance, human legs provide stabilizing torques that can be modeled as a spring-damper mechanical impedance. While powered prosthetic legs can also imitate spring-damper behaviors, the rendered impedance can be quite different from the achieved impedance thanks to friction in the transmission. Moreover, for powered prostheses to mimic the human's impedance, which varies widely between stance and swing, they will need to accurately render this wide range of mechanical impedance in a variety of ground contact conditions. In particular, this requires nearly free-swinging behavior in swing and stiff spring-like behavior in stance. For low-cost series-elastic prosthetic legs with nontrivial transmission kinetics, e.g. the Open Source Leg, this presents a challenge for traditional impedance control. In this paper we propose a solution based on disturbance observers and full state feedback impedance control. The disturbance observer can suppress the nonlinear friction of the transmission, the root cause of actuator non-backdrivability, independent of the chosen impedance. With this effect eliminated, the FSF controller can reproduce a wide range of mechanical impedance behaviors through a well-understood process of pole-zero placement. We validate our control framework on a two-actuator dynamometry testbed designed to mimic the OSL.

I. INTRODUCTION

Loss of a lower limb prevents millions of Americans from performing activities of daily life, with millions more projected in the coming years [1]. Amputation of the lower limbs results in a corresponding loss in power-producing muscles, e.g. the foot plantarflexors which generate up to 80% of the mechanical power for gait [2]. Passive prostheses, which are inherently unable to generate net positive work, therefore rely upon compensations by intact proximal joints and muscles to offset this loss of power [2]. Unfortunately, such compensations introduce complications such as osteoarthritis [3], and chronic back pain [4]. Powered prosthetic devices have shown promise in recovering this lost functionality [5] and are consistently improving in power-density, weight, battery life, and recognition of human intent. However, the state-of-the-art in powered prosthetic legs is still limited by both mechanical design and feedback control, which can lead to disuse of devices, fear of falling [6] and avoidance of activities [7].

Platforms like the Open Source Leg [5] are vehicles for research into the control aspects of these limitations, and they provide the low-level control abstraction layers that are necessary for testing high-level feedback control ideas. The design of this abstraction layer is important both for allowing the high level controller to accurately control the mechanical impedance of the device, and for allowing high level controllers to eventually be ported across devices, for example from the research platform to the eventual clinical device. This second requirement means that the control interface provided should be agnostic to the particular parameters of the device on which it was designed.

One highly-desirable low-level interface is to provide a biomechanically motivated torque-position trajectory representing the expected leg behavior alongside a *mechanical impedance* [8] that describes what happens in response to unexpected deviations from this behavior. This generalizes simpler notions of position or torque control, which represent the limiting behaviors as the mechanical impedance approaches the respective extremes of an immovable joint or a perfect torque source. However, biomimetic mechanical impedance tracking is not available on most research prostheses, and remains a gap between today's prosthetic legs and real human legs. A proper impedance control interface would need to ensure accurate rendering of the output impedance, and additionally remove the nonlinear effects of transmission friction.

Series elastic actuators are a key mechanism for allowing low-cost prosthetic legs to render mechanical impedance [9].[1] And the Open Source Leg [12] is built with series elastic actuators for this purpose. Control of SEAs [9] and more generally, flexible joint robots [13], differs from traditional actuator control in that the impedance [14] is directly measurable and can be controlled by feedback of both the spring deflection (or torque) and the motor or joint position. This impedance control problem can be framed either as specifying a torque for any position (an impedance) or specifying a position for any torque (an admittance), and these two ways of viewing the problem lend themselves to two popular cascaded control approaches for the problem, with the inner-loop comprising, respectively, a spring deflection controller or a motor position controller. However, the cascade control assumption—that the inner loop have higher bandwidth than the outer loop—restricts the capabilities of each of these models [15]. Impedance control cascades are good at rendering soft impedances, and admittance control cascades are good at rendering hard impedances, but both are restricted in range—especially when the real systems

[1] Mechanical Engineering, University of Michigan, Ann Arbor, MI 48109, USA

[2] Bernard D. Researcheris with the Department of Computer Science and Electrical Engineering, University of Michigan, Ann Arbor, MI 48109, USA
   *gcthomas@ieee.org

[1] They also have other benefits, including energy recovery during walking [10], [11].

suffers from common nonlinear disturbances like transmission friction. Since a wide range of impedance behaviors are necessary to mimic human walking, this is a limitation of the cascaded approach.

Neglecting the nonlinear effects of the belt dynamics and the adjustable spring assembly, impedance control is a well-studied problem in control. The full state feedback controller pioneered by the German aerospace instutute (DLR) uses full state feedback to change the natural impedance of the actuator within a wide range including both extremely soft and extremely stiff designs [16]. While many controllers designed to render a single impedance adopt a cascaded approach of either inner loop force or position control, this design approach avoids the limitations of the cascade control frequency separation condition [15]. However, the lack of a high bandwidth inner loop can result in controllers that do not significantly attenuate the friction disturbance, especially when rendering impedances similar to the natural impedance of the actuator.

To deal with the non-ideal behavior of real hardware, recent SEA controllers have been equipped with disturbance compensating filters known as disturbance observers. Disturbance observers work by indirectly measuring the disturbances to a nominal plant $G(s)$ and compensating for this. The measurement is achieved by comparing low pass ($Q(s)$) filtered plant input to low pass filtered plant output that has gone through a plant-inverse filter (the combination of the low pass filter and the plant-inverse filter allows the combined system $Q(s)G^{-1}(s)$ to be a causal system). The framework then feeds the estimate of input disturbance back into the input of the plant, compensating for the effects of the disturbance completely at frequencies where $Q(s) \approx 1$. These techniques have been central to some of the most state-of-the-art performance, both in cascaded [17], [18] and full state feedback [19] controllers. While handling SEA imperfections can also be approached from the robust control perspective [20], [21], the disturbance observer technique conveniently reduces the magnitude of the non-linearity in the plant to improve the performance of standard linear control without requiring a controller redesign. Refs. [19], [22] have shown promising results combining disturbance observers for transmission friction with full state feedback controllers, however both systems took a continuous-time approach that is not well matched to our sample rate and desired behaviors.

The recently developed Open-Source Leg offers a unique opportunity to integrate this emerging control paradigm in a universal testbed with series elastic actuators that soften interactions between the user, prosthesis, and environment. We seek to understand how to achieve closed-loop torque and impedance control in the series elastic actuator of the open-source leg despite unmodeled dynamics from its low-cost design. And we approach this problem using the Michigan SEA testbed hardware which simulates the transmission and spring-carriage of the OSL.

In this paper, we 1) present a new discrete-time frequency-domain framework for torque and impedance control of

TABLE I
SYMBOL GLOSSARY

Symbol	Meaning
ϕ_a	knee motor position
ϕ_j	environment motor position
θ_a, θ_j	motor signals reflected through transmission
N	transmission ratio
J, b	inertia and damping, motor-frame
τ_s	spring torque
V_a, I_a	motor voltage and current
R	motor electrical resistance
K_t	motor torque constant
K_s	spring stiffness
K_1, B_1, K_2, B_2	controller parameters (constant)
$\tilde{K}_1, \tilde{B}_1, \tilde{K}_2, \tilde{B}_2$	compliance shape parameters (constant)

the series elastic actuators in the OSL, 2) demonstrate the elimination of parasitic effects from imperfect transmissions, and 3) demonstrate successful superposition of a mechanical impedance on top of a biomechanical position and torque trajectory tracking.

II. MODELING AND CONTROL

A. System and Test Apparatus

The testbed simulates two systems: the OSL's series-elastic knee actuator and the rest of the environment in which it is designed to operate (see Fig. 1), *i.e.*, the residual limb of a transfemoral amputee moving through a periodic walking behavior with intermittent ground contact. The simulated SEA consists of three parts: 1) an OSL BLDC motor (ActPack, Dephy Inc. Boston, MA), 2) a 50:1 Gearbox (Boston Gear, Boston, MA) which matches the transmission ratio of the OSL knee, and 3) the OSL torsional spring carriage assembly [5]. The residual limb is simulated by another OSL BLDC motor and 50:1 Gearbox. Identical to the OSL's embedded system, a Raspberry Pi computer orchestrates the high-level voltage commands sent to each motor's control board.

We model the continuous dynamics of the SEA as

$$J\ddot{\phi}_a = K_t I_a - b\dot{\phi}_a + \tau_s, \tag{1}$$

$$V_a = RI_a + K_t \dot{\phi}_a, \tag{2}$$

$$\tau_s = K_s(\theta_j - \theta_a), \tag{3}$$

$$\phi_a = N\theta_a, \ \phi_j = N\theta_j, \ N = 50 \tag{4}$$

with variables as defined in Tab. I. Essentially, an ideal DC motor, (1) and (2), are coupled by a spring (3) on the other side of corresponding transmissions [**?**]. The DC approximation of the brushless DC motors is made possible by the q-axis DC representation [23]. Combining (1-4) and applying the Laplace Transform, the transfer function from input V_a to output ϕ_a (and for input V_j to output ϕ_j) is

$$G(s) = \frac{K_t N R^{-1}}{Js^2 + (b + K_t^2 R^{-1})s + K_s N^{-2}}, \tag{5}$$

and the gain from the auxiliary input ϕ_j (and for ϕ_a) to its equivalent representation as a voltage is

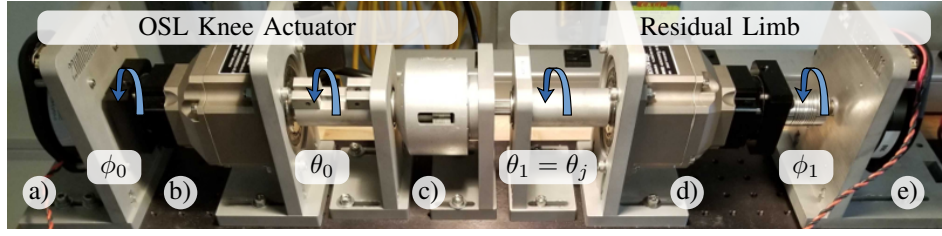$$\Psi = \frac{RK_s}{K_t N^2}. \tag{6}$$

Fig. 1. Time domain results

Together, (5-6) provide an actuator model with two inputs: commanded motor voltage, V_a, and joint angle, ϕ_j (see Fig. 2). Note that (6) converts ϕ_j to an effective voltage felt by the motor (*i.e.*, the change in motor voltage that would produces the same change in motor acceleration as this change in spring output position).

B. Controller

The impedance controller consists of three parts: (1) a nominal trajectory generator, (2) a disturbance observer for cancelling nonlinearities, and (3) a full state feedback controller used to achieve bio-mimetic impedance.

1) Nominal Trajectory Generation: The goal of the nominal trajectory generator is to produce the a-priori voltage signal time series for the two motors, $u_k \in \mathbf{R}^2$, that will achieve desired joint angle and joint torque trajectories, y_k, in the absence of disturbances and nonlinearities. This becomes a non-trivial model inversion problem which can be achieved by analyzing the coupled dynamics of both motors in state space representation given by the LTI system

$$\begin{aligned}\dot{x} &= Ax + Bu, \\ y &= Cx,\end{aligned} \quad (7)$$

where

$$A = \begin{bmatrix} 0 & 1 & 0 & 0 \\ -\alpha & \beta & \alpha & 0 \\ 0 & 0 & 0 & 1 \\ \alpha & 0 & -\alpha & \beta \end{bmatrix}, \quad x = \begin{bmatrix} \phi_a \\ \dot{\phi}_a \\ \phi_j \\ \dot{\phi}_j \end{bmatrix},$$

$$B = \frac{K_t}{JR}\begin{bmatrix} 0 & 0 \\ 1 & 0 \\ 0 & 0 \\ 0 & 1 \end{bmatrix}, \quad u = \begin{bmatrix} V_a \\ V_j \end{bmatrix},$$

$$C = \frac{1}{N}\begin{bmatrix} -K_s & 0 & K_s & 0 \\ 0 & -K_s & 0 & K_s \\ 0 & 0 & 1 & 0 \\ 0 & 0 & 0 & 1 \end{bmatrix}, \quad y = \begin{bmatrix} \tau_s \\ \dot{\tau}_s \\ \theta_j \\ \dot{\theta}_j \end{bmatrix},$$

and

$$\alpha = {}^{K_s}/{JN^2}, \quad \beta = -J^{-1}(b + {}^{K_t^2}/R). \quad (8)$$

To account for the delay between consecutive motor voltage commands, we convert (7) to a discrete time representation with a ZOH on the input and sample time, T_s

(i.e. voltage commands are assumed constant between time steps). The discretized model is given by

$$x_{k+1} = A_k x_k + B_k u_k, \quad (9)$$
$$y_k = C x_k, \quad (10)$$

where the discrete-time matrices can be calculated according to a zero-order hold assumption on the input as

$$A_k = e^{AT_s}, \quad (11)$$
$$B_k = \int_0^{T_s} e^{A\tau} B \, d\tau. \quad (12)$$

Next, to find the voltage signals which correspond to nominal joint angle and joint torque trajectories, we must invert (9). There are multiple strategies which yield satisfactory y_k, but given the digital nature of our controller, we utilized the discrete-time controllability matrix, M_n, where

$$M_n = \begin{bmatrix} B_k, & A_k B_k, & \cdots, & A_k^{n-1} B_k \end{bmatrix}, \quad (13)$$

for an n-step ahead state prediction. If M_n has full row rank (*i.e.*, $\mathrm{rank}(M_n) = \dim(x_k) = 4$), then x_{k+n} can be arbitrarily placed. Ideally, we would like full control over x_{k+1}, but the corresponding controllability matrix, $M_1 = B_k$, only has rank 2. To achieve full row rank, we loosen our constraint to full controllability of x_{k+2} which is given by

$$x_{k+2} = A_k^2 x_k + B_k u_{k+1} + A_k B_k u_k, \quad (14)$$
$$M_2 = \begin{bmatrix} B_k, & A_k B_k \end{bmatrix}. \quad (15)$$

Since M_2 is full row rank, it permits model inversion. Taking advantage of the fact that C is square and invertible, we rewrite (14) using (10) and (15) to obtain the input vector $\hat{u} \in \mathbb{R}^4$ where

$$\hat{u} = \begin{bmatrix} u_{k+1} \\ u \end{bmatrix} = M_2^{-1}(C^{-1} y_{k+2} - A_k^2 C^{-1} y_k), \quad (16)$$

i.e., the exact solution for the discrete feedforward input that brings the system output from y_k to y_{k+2}. While this inversion method technically only provides half the desired resolution in our output signal, for small sample times and continuous target behaviors, $y[m]$ approaches the desired signal, $y[n]$.
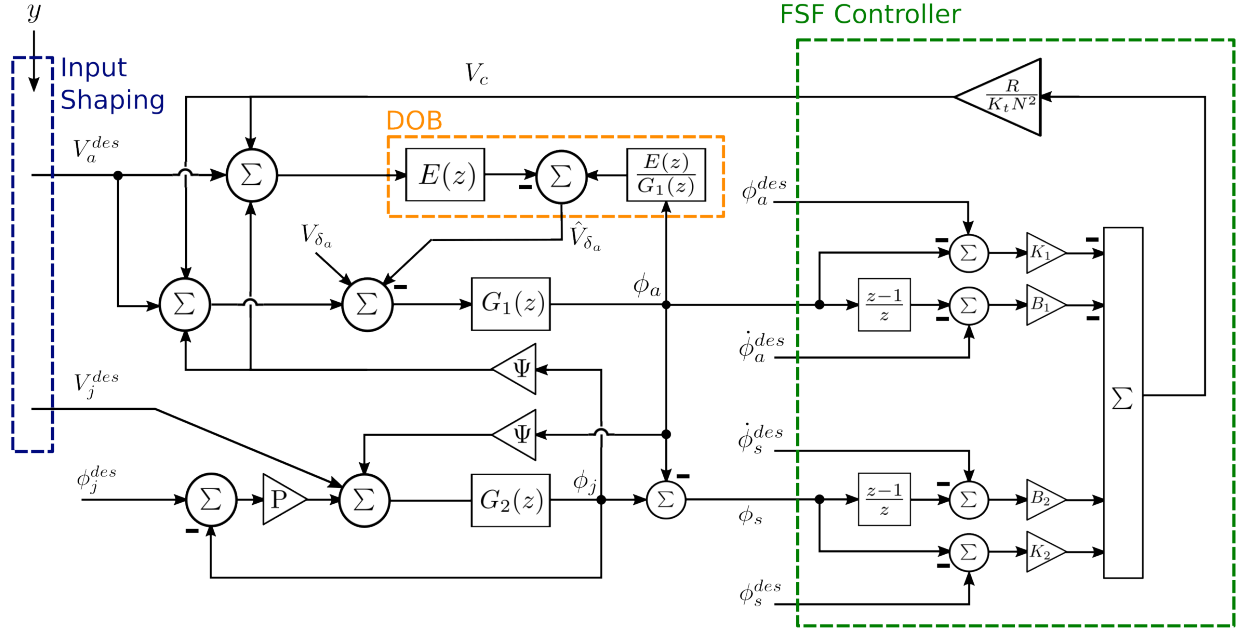
Fig. 2. Controller Block Diagram, where y contains a-priori joint trajectories defined by (7), and desired feed forward voltages, V_a^{des} and V_j^{des}, are calculated using (16). Note, the simple discrete derivative operator, $(1-z^{-1})$, is used in the block diagram, but in practice we used filtered motor velocities provided by the Dephy ActPack

2) Disturbance Observer: A disturbance observer (DOB) wraps the nominal actuator model given by (5), allowing the feedforward trajectory generator and full state feedback controller to assume a pristine model without nonlinearities and other imperfections. The largest unmodeled nonlinearity present in our testbench is static friction from the gear boxes. Additionally, there is plant uncertainty in the estimates of K_t, b, J, R, *etc.*.

Using (5) and (6), a typical continuous-time DOB can be constructed for the actuator model which has the following form,

$$\hat{V}_{\delta_a} = \frac{Q(s)}{G(s)}\phi_a - Q(s)(V_a^{des} + \Psi\phi_j - \hat{V}_{\delta_a}), \qquad (17)$$

where $Q(s)$ is a second order low pass filter with cutoff frequency w, and damping ratio ζ, whose transfer function is

$$Q(s) = \frac{w^2}{s^2 + 2\zeta w + w^2}. \qquad (18)$$

This low pass filter serves the dual purpose of reducing high frequency measurement noise and preserving causality despite inverting G. The DOB's output, $\hat{V}_{\delta_a}$, can be subtracted from the voltage effort issued by the FF and FSF controllers, V_a^{des}, to cancel any effects that nonlinearities and uncertainties would otherwise have on the output.

To adapt this continuous-time DOB to our digital control system, we solve (17) for $\hat{V}_{\delta_a}$

$$\hat{V}_{\delta_a} = \frac{E(s)}{G(s)}\Theta_a - E(s)(V_a^{des} + \Psi\Theta_p), \qquad (19)$$

$$E(s) = \frac{1}{Q^{-1} - 1}. \qquad (20)$$

Next we obtain the discrete transfer function, $E(z)$, by a three step process: 1) convert $E(s)$ to state space controllable canonical form, 2) use (11) and (12) to obtain discrete matrices, and 3) convert back to transfer function representation. The same process is applied to $G(s)$ to obtain $G(z)$ which then allows us to write the full expression for the discrete DOB output as

$$\hat{V}_{\delta_a} = \frac{E(z)}{G(z)}\Theta_a - E(z)(V_a^{des} + \Psi\Theta_p), \qquad (21)$$

which is shown in context in Fig. 2.

C. Full State Feedback Compliance Shaping

1) Control Structure: To accurately render biomimetic impedance, we adopt the full state feedback with compliance shaping paradigm developed in [24]. This method revolves around manipulating the gains of a full state feedback (FSF) control law with following structure:

$$V_c = \frac{R}{K_t N^2}((K_2 + B_2 s)\Delta\phi_s - (K_1 + B_1 s)\Delta\phi_a), \quad (22)$$

$$\Delta\phi_s = \Delta\phi_j - \Delta\phi_a, \quad \Delta\phi = \phi^{des} - \phi. \qquad (23)$$

By feeding back the entire state, we can place the poles and zeros of the actuator compliance transfer function $\frac{\theta_j}{\tau_s}(s)$ wherever we desire. This transfer function is

$$\frac{\theta_j}{\tau_s} = \frac{\hat{J}s^2 + (\hat{b} + B_1 + B_2)s + (K_s + K_1 + K_2)}{(\hat{J}s^2 + (\hat{b} + B_1)s + K_1)K_s}, \qquad (24)$$

where

$$\hat{J} = JN^2, \quad \hat{b} = bN^2 + K_t^2 N^2 R^{-1}. \qquad (25)$$

To construct (24), one can use (1-4) where (2) is equal to the new FSF control law given by (22).

Changing variables as in Ref. [22], we obtain its monic form (which lends itself to frequency domain tuning),

$$\frac{\theta_j}{\tau_s} = \frac{s^2 + \tilde{B}_2 s + \tilde{K}_2}{(s^2 + \tilde{B}_1 s + \tilde{K}_1)K_s}, \tag{26}$$

where

$$K_1 = \hat{J}\tilde{K}_1, \quad K_2 = \hat{J}\tilde{K}_2 - \tilde{K}_1 - K_s,$$
$$B_1 = \hat{J}\tilde{B}_1 - \hat{b}, \quad B_2 = \hat{J}\tilde{B}_2 - B_1 - \hat{b}. \tag{27}$$

Ultimately, this controller is used to shape the closed loop joint compliance

$$\frac{\theta_j}{\tau_j} = \frac{s^2 + \tilde{B}_2 s + \tilde{K}_2}{J_j s^2(s^2 + \tilde{B}_2 s + \tilde{K}_2) + K_s(s^2 + \tilde{B}_1 s + \tilde{K}_1)}, \tag{28}$$

so that it emulates the compliance of a biological knee joint

$$C_k(s) = \frac{1}{J_k s^2 + B_k s + K_k}. \tag{29}$$

2) Frequency Domain Shaping: The controller gains present in (26) were tuned by analyzing its transfer function in the frequency domain. The design space is constrained by four factors: 1) the target knee stiffness, K_k, which necessitates a low frequency asymptote equal to K_k^{-1}, 2) the target knee damping, B_k, which governs the placement of a low frequency pole, 3) the stiffness of the physical series elastic element, K_s, which necessitates a high frequency asymptote equal to K_s^{-1}, and 4) the practical limitation of the controller's update rate, f_u equal to 450 Hz and the related Nyquist frequency of $f_u/2$. Since most of the poles and zeros in the resulting system will be achieved via delayed feedback, we intentionally limit these pole and zero placements to be well below the Nyquist frequency at 50 Hz.

We start by choosing our two poles, with the lower frequency pole, p_1, being given directly by the target biological impedance, and the high frequency pole, p_2, at 50 Hz,

$$p_1 = \frac{K_k}{B_k}, \quad p_2 = \frac{\pi f_u}{4}. \tag{30}$$

Given the asymptotic high and low frequency behaviors, these two poles define two lines that cross in the Bode plot. We connect these two lines with a pair of critically damped zeroes

$$\omega_z = \sqrt{\frac{1}{DB_k}}, \quad D = \frac{1}{K_s p_2}. \tag{31}$$

Finally, we can extract the gains which comprise (26) using the following relationships

$$\tilde{K}_1 = p_1 p_2, \quad \tilde{B}_1 = p_1 + p_2, \tag{32}$$
$$\tilde{K}_2 = \omega_z^2, \quad \tilde{B}_2 = 2\omega_z, \tag{33}$$

which can subsequently be used with (27) to obtain the final set of gains present in our FSF control law given by (22).

TABLE II
EXPERIMENT PARAMETERS

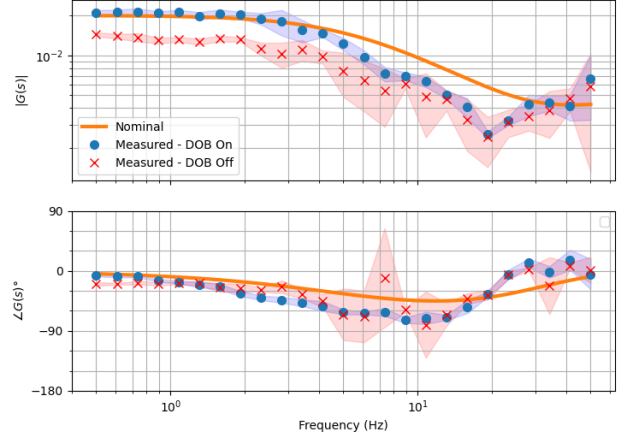| Symbol	Value
K_1	4932.9
B_1	-5.7
K_2	13719.7
B_2	21.4
K_k	50.0
B_k	1.59

Fig. 3.   Frequency domain results

III. METHODS

Both frequency domain and time domain experiments were performed to analyze controller performance. During all experiments, ϕ_a and ϕ_j were measured using the embedded motor encoders, which were poled at 450 Hz. From those two measurements, both τ_j, and θ_j, can be calculated using (3) and (4).

A. Frequency-Domain Validation

To measure the actual joint compliance rendered by our controller, a frequency domain experiment was performed, To simulate perturbations in joint angle, θ_j, wavelets of varying frequency were applied to the Knee Actuator via the Environment Actuator. Each wavelet was generated with a single frequency component ranging from 0.5 to 50 Hz, and an amplitude of 0.1 radians. In between wavelets, a minimum pause of 2 seconds was included to allow the Knee Actuator to come to rest prior to the next perturbation. Following the experiment, a least squares method was used to convert τ_j, and θ_j, from time series data to their respective phasor representations in the complex plane. From here, it is straight forward to obtain magnitude and phase measurements.....

B. Time-Domain Validation

A time domain test was conducted to demonstrate controller performance when subjected to biological knee signals. Joint angle and joint torque during level walking were used as the nominal trajectories. These signals were generated using data from X database, assuming a 1.2 second
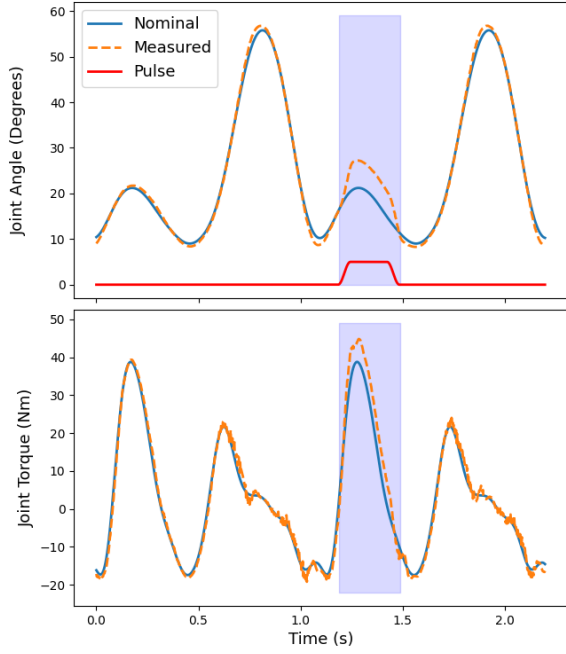
Fig. 4. Level Walking Simulation

walking period, and 80kg body mass. Both an undisturbed, and disturbed step were simulated for comparison. The disturbance was applied at the beginning of stance as a 3 second pulse in joint angle, with a 5 degree amplitude.

IV. RESULTS

A. Frequency-Domain Results

The frequency-domain experiment shows that the DOB improves mechanical impedance rendering performance (Tab. III). Of particular interest is the controller performance below half the DOB filter cutoff frequency, f_q (i.e. where the filter's magnitude ≈ 1). In that range, the FSF + DOB controller rendered a mechanical impedance with a magnitude RMSPE of 11.8% and phase RMSE of $14.9°$. Compared to the no DOB case, the magnitude error was nearly three times smaller, with negligible difference in phase. At the lowest frequency tested, $f = 0.5$ Hz, the FSF + DOB controller yielded even better results, achieving an RMSPE magnitude of 7.2% and only $2.88°$ of phase lag.

B. Time-Domain Results

The time domain simulation clearly demonstrates the two-fold capability of the controller: 1) it successfully tracks knee angle and torque trajectories during nominal conditions and 2) it accurately renders the desired biological impedance when the joint experiences a disturbance. While this type of dual controller has been implemented previously in other related fields (e.g. exoskeletons [22], industrial robots [citation]), to the author's knowledge it has not been implemented on lower limb prosthesis.

To analyze the accuracy of impedance rendering, we begin by defining another delta term

$$\Delta\theta_s = \theta_{s,p} - \theta_{s,u} \tag{34}$$

where the secondary subscripts, p and u, denote perturbed and unperturbed steps respectively. Note, (34) compares measured values from two different steps, while (23) compares a measured value with a desired value for the same time sample. Next, we compute the difference in measured spring torque between the nominal and perturbed steps, $\Delta\tau_s$, which is given by,

$$\Delta\tau_s = K_s\Delta\theta_s \tag{35}$$

and the difference in ideal knee torque, $\Delta\tau_k$ (i.e. the torque that would occur if the system exhibited the ideal knee impedance), which is given by

$$\Delta\tau_k = K_k\Delta\theta_s + B_k\Delta\dot{\theta}_s \tag{36}$$

Finally, our impedance accuracy is given by the error between those torque quantities

$$\epsilon_\tau = \Delta\tau_k - \Delta\tau_s \tag{37}$$

whose RMS value was found to be 2.35 Nm.

V. DISCUSSION

The DOB improved the rendering of mechanical impedance in the simulated prosthetic application, yielding significant reductions in both magnitude and phase errors. It performed especially well at low frequencies, achieving an RMSPE magnitude error of 7.2%.

These results are significantly better than state of the art open loop impedance control performed in [25], which showed stiffness errors that reached up to 42% when the actuator included a large transmission ratio. While the authors did discuss a solution capable of reducing stiffness errors to a mere 2.9%, it required characterizing disturbances offline and manually tuning feed forward correction factors. This strategy also compensated for the nonlinear disturbance by changing the linear controller, without necessarily evaluating how this would impact performance at magnitudes other than the one tested in their system identification. In contrast, our DOB framework provides a way to accurately reject nonlinear friction disturbances online, and also bypasses the need for extensive characterization and tuning. While we also only perform system identification at a single frequency, the disturbance observer is capable of rejecting nonlinear disturbances.

Additionally, the smallest change in knee stiffness a human can reliably detect is approximately 13% [26]. Therefore, the controller RMSPE error for frequencies lower than 5 Hz can be said to be below this perceptual threshold with the DOB and above it without. However, it should be noted that at about $f = 1$ Hz the compliance magnitude begins to decrease indicating that damping is also beginning to contribute so it is no longer directly comparable to the stiffness metric in [26]. It is also unclear how the $14.9°$ of phase lag would affect a human's perception of the rendered impedance.

TABLE III

FREQUENCY DOMAIN TEST RESULTS

Freq Range (Hz)	$f = 0.5$		$0.5 \leq f \leq 5$		$0.5 \leq f \leq 50$	
DOB Used	Yes	No	Yes	No	Yes	No
RMSPE Magnitude	7.2%	28.0%	11.8%	34.7%	31.1%	46.2%
RMSE Phase (Deg)	$2.88°$	$15.6°$	$14.9°$	$12.2°$	$21.7°$	$30.1°$

The cutoff frequency of the DOB played a significant and unexpected role in the stability of the controller. In theory, we should have been able to increase f_q up to the Nyquist frequency at $225Hz$ without impacting the stability and independent of the FSF gains or chosen trajectory. But in practice this did not hold. By trial and error, the system was found to be stable for $f_q \leq 10Hz$ during the frequency domain wavelet tests, and $f_q \leq 5Hz$ for the level walking time domain test. This may be due to the assumption that the disturbance is uncorrelated with the state vector, which is likely not held in practice. The chief disturbance appears to have been Coulomb friction, which is almost like a DC bias torque in the system except that it changes sign when the velocity does. Our low-frequency DOB was certainly helpful in reducing the effect of this disturbance on rendered impedance below this cutoff frequency, but future versions of the system should be able to achieve better performance by investigating the bandwidth limit on the DOB more carefully and re-considering or working around the independence assumption on the disturbance.

Different FSF controller settings produce different levels of sensitivity to the transmission friction, and therefore different levels of importance for the DOB which compensates for this friction. High impedance behaviors that result from greater utilization of the spring feedback terms K2 and B2, will naturally attenuate the friction disturbance due to this spring feedback alone. And negative spring feedback gains (used to produce stiffer-than-passive impedance) amplify the disturbance. Thus, by careful design of the actuator it may be possible to avoid the DOB component of the controller, and (equivalently), by introducing a DOB it may be possible to overcome the mechanical limits of a design.

The profile we simulated represents a knee following a normative level-ground walking behavior where the knee flexes during stance. This could be considered a very ambitious behavior, since people with amputation are trained today to use only gaits which mechanically lock the knee during stance for 'stability' (i.e., to ensure that the knee does not collapse under them). To achieve stance with a flexed knee, the mechanical stiffness of the knee joint must exceed a minimum stiffness to counteract the unstable buckling dynamic. And this highlights the importance of mechanical impedance matching in prosthetic legs that recreate biological kinematics.

REFERENCES

[1] K. Ziegler-Graham, E. J. MacKenzie, P. L. Ephraim, T. G. Travison, and R. Brookmeyer, "Estimating the prevalence of limb loss in the united states: 2005 to 2050," *Archives of physical medicine and rehabilitation*, vol. 89, no. 3, pp. 422–429, 2008.

[2] D. A. Winter, "Energy generation and absorption at the ankle and knee during fast, natural, and slow cadences," *Clinical Orthopaedics and Related Research®*, vol. 175, pp. 147–154, 1983.

[3] J. Kulkarni, J. Adams, E. Thomas, and A. Silman, "Association between amputation, arthritis and osteopenia in british male war veterans with major lower limb amputations," *Clinical Rehabilitation*, vol. 12, no. 4, pp. 348–353, 1998.

[4] J. Kulkarni, W. Gaine, J. Buckley, J. Rankine, and J. Adams, "Chronic low back pain in traumatic lower limb amputees," *Clinical rehabilitation*, vol. 19, no. 1, pp. 81–86, 2005.

[5] A. F. Azocar, L. M. Mooney, J.-F. Duval, A. M. Simon, L. J. Hargrove, and E. J. Rouse, "Design and clinical implementation of an open-source bionic leg," *Nature Biomedical Engineering*, pp. 1–13, 2020.

[6] W. Miller, A. Deathe, M. Speechley, and J. Koval, "The influence of falling, fear of falling, and balance confidence on prosthetic mobility and social activity among individuals with a lower extremity amputation," *Arch. Phys. Med. Rehab.*, vol. 82, no. 9, pp. 1238–1244, 2001.

[7] B. J. Hafner and D. G. Smith, "Differences in function and safety between medicare functional classification level-2 and-3 transfemoral amputees and influence of prosthetic knee joint control." *Journal of Rehabilitation Research & Development*, vol. 46, no. 3, 2009.

[8] E. J. Rouse, R. D. Gregg, L. J. Hargrove, and J. W. Sensinger, "The difference between stiffness and quasi-stiffness in the context of biomechanical modeling," *IEEE Transactions on Biomedical Engineering*, vol. 60, no. 2, pp. 562–568, 2012.

[9] G. A. Pratt and M. M. Williamson, "Series elastic actuators," in *Proceedings 1995 IEEE/RSJ International Conference on Intelligent Robots and Systems. Human Robot Interaction and Cooperative Robots*, vol. 1. IEEE, 1995, pp. 399–406.

[10] M. Grimmer and A. Seyfarth, "Stiffness adjustment of a series elastic actuator in an ankle-foot prosthesis for walking and running: The trade-off between energy and peak power optimization," in *2011 IEEE International Conference on Robotics and Automation*. IEEE, 2011, pp. 1439–1444.

[11] E. J. Rouse, L. M. Mooney, and H. M. Herr, "Clutchable series-elastic actuator: Implications for prosthetic knee design," *The International Journal of Robotics Research*, vol. 33, no. 13, pp. 1611–1625, 2014.

[12] A. F. Azocar, L. M. Mooney, J.-F. Duval, A. M. Simon, L. J. Hargrove, and E. J. Rouse, "Design and clinical implementation of an open-source bionic leg," *Nature biomedical engineering*, vol. 4, no. 10, pp. 941–953, 2020.

[13] M. W. Spong, "Modeling and control of elastic joint robots," *Journal of dynamic systems, measurement, and control*, vol. 109, no. 4, pp. 310–319, 1987.

[14] N. Hogan, "Impedance control: An approach to manipulation: Part ii—implementation," *Journal of Dynamic Systems, Measurement, and Control*, vol. 107, no. 1, pp. 8–16, 1985.

[15] C. Ott, A. Albu-Schäffer, A. Kugi, and G. Hirzinger, "On the passivity–based impedance control of flexible joint robots," *IEEE Transactions on Robotics*, vol. 24, no. 2, pp. 416–429, 2008.

[16] A. Albu-Schäffer and G. Hirzinger, "State feedback controller for flexible joint robots: A globally stable approach implemented on dlr's light-weight robots," in *Intelligent Robots and Systems, 2000.(IROS 2000). Proceedings. 2000 IEEE/RSJ International Conference on*, vol. 2. IEEE, 2000, pp. 1087–1093.

[17] K. Kong, J. Bae, and M. Tomizuka, "Control of rotary series elastic actuator for ideal force-mode actuation in human–robot interaction applications," *IEEE/ASME Transactions on Mechatronics*, vol. 14, no. 1, pp. 105–118, Feb 2009.

[18] N. Paine, S. Oh, and L. Sentis, "Design and control considerations for

high-performance series elastic actuators," *IEEE/ASME Transactions on Mechatronics*, vol. 19, no. 3, pp. 1080–1091, 2014.

[19] L. Le-Tien, A. Albu-Schäffer, A. De Luca, and G. Hirzinger, "Friction observer and compensation for control of robots with joint torque measurement," in *2008 IEEE/RSJ International Conference on Intelligent Robots and Systems*. IEEE, 2008, pp. 3789–3795.

[20] K. Haninger, J. Lu, and M. Tomizuka, "Robust impedance control with applications to a series-elastic actuated system," in *Intelligent Robots and Systems (IROS), 2016 IEEE/RSJ International Conference on*. IEEE, 2016, pp. 5367–5372.

[21] G. C. Thomas and L. Sentis, "MIMO identification of frequency-domain unreliability in SEAs," in *American Control Conference (ACC), 2017*. IEEE, May 2017, pp. 4436–4441.

[22] G. C. Thomas, J. M. Coholich, and L. Sentis, "Compliance shaping for control of strength amplification exoskeletons with elastic cuffs," in *2019 IEEE/ASME International Conference on Advanced Intelligent Mechatronics (AIM)*. IEEE, 2019, pp. 1199–1206.

[23] U. H. Lee, C.-W. Pan, and E. J. Rouse, "Empirical characterization of a high-performance exterior-rotor type brushless dc motor and drive," in *2019 IEEE/RSJ International Conference on Intelligent Robots and Systems (IROS)*. IEEE, 2019, pp. 8018–8025.

[24] G. C. Thomas, J. S. Mehling, J. Holley, and L. Sentis, "Phase-relaxed-passive full state feedback gain limits for series elastic actuators," *IEEE/ASME Transactions on Mechatronics*, vol. 26, no. 1, pp. 586–591, 2020.

[25] A. F. Azocar and E. J. Rouse, "Characterization of open-loop impedance control and efficiency in wearable robots," *IEEE Robotics and Automation Letters*, vol. 7, no. 2, pp. 4313–4320, 2022.

[26] ——, "Stiffness perception during active ankle and knee movement," *IEEE Transactions on Biomedical Engineering*, vol. 64, no. 12, pp. 2949–2956, 2017.